Author for correspondence:
Frantz Maerten, Email: fmaerten@gmail.com

Joint inversion of tectonic stress and magma pressures using dyke trajectories

F. Maerten[1] ⓘ, L. Maerten[1], R. Plateaux[2] and P. H. Cornard[3]

[1]YouWol, Le Lancaster, 455 rue Alfred Sauvy, Pérols 34470, France; [2]Open Plateau Ltd, F14-3, N57, Fuxing North Road, Songshan District Taipei City 105, Taipei, Taiwan and [3]Department of Geology, University of Innsbruck, Innrain 52, Innsbruck, Austria

Abstract

In volcano-tectonic regions, dyke propagation from shallow magmatic chambers is often controlled by the interaction of the local and regional stress fields. The variations of the stress fields result from a combination of factors including the regional tectonic stress, the geometry of pressurized magma chambers, the layering and the pre-existing discontinuities (e.g. fractures). In this contribution, we describe and apply a new multiparametric inversion technique based on geomechanics that can invert for both the far field stress attributes and the internal pressure of magma chambers or stocks, constrained by observed dyke or eruptive fissure orientations. This technique is based on the superposition principle and uses linear elastic models that can be solved using many types of numerical methods. For practical reasons, we chose a 3D boundary element method (BEM) for a heterogeneous elastic half-space, where magma chambers are modelled as pressurized cavities. To verify this approach, the BEM solution has been validated against the known 3D analytical solution of a pressurized cylindrical cavity. Then the effectiveness of this technique and its practical use is demonstrated through application to natural examples of dyke network development around two different volcanic systems, the Spanish Peaks (USA) and the Galapagos Islands (Ecuador). Results demonstrate that regional stress characteristics as well as the internal pressure of magma chambers can be estimated from observed radial and circumferential dyke patterns and some knowledge of magma chamber geometry.

1. Introduction

Crustal stress within volcano-tectonic settings is the result of a combination of regional tectonic stresses, the geometry of local pressurized magma bodies (Pollard & Muller, 1976; Gudmundsson, 2020) and the mechanical properties of the host rock, in particular associated to layering (Bazargan & Gudmundsson, 2019, 2020). The nature of the competing interactions between tectonic and volcanic processes remains a challenge to understand due to the different space and time windows in which they occur. Progress in understanding the interplay between tectonic and volcanic processes has been made using modern techniques such as geodetic, photogrammetric and geological surveys (Knopf, 1936; Chadwick & Howard, 1991), as well as investigations of crustal stress using theoretical models (Yamakawa, 1955; Mogi, 1959; Pollard, 1987; Okada, 1992; Rubin, 1995; Pinel & Jaupart, 2004; Gudmundsson & Andrew, 2007).

A typical volcanic system consists of a volcanic edifice, perhaps associated with a collapse caldera, an active shallow magma chamber supplying the edifice with magma through dykes, and a deeper magma accumulation zone or magma reservoir (Fig. 1). When the pressure of the magma chamber exceeds the host rock strength, dykes will initiate and propagate toward the surface, either reaching it as eruptive fissures or being arrested or deflected into sills (Gudmundsson, 2012). As they find their way to the surface, dykes will propagate orthogonal to the minimum local principal stress (Anderson, 1951). They are therefore markers of past or present-day spatially heterogeneous stress fields in volcanic regions (Nakamura *et al.* 1977; Chadwick & Howard, 1991; Rubin, 1995). Consequently, dykes appear to be ideal candidates for recovering past or present-day stress fields that result from the interaction of tectonic stress and the driving pressure in magma chambers (Odé, 1957; Muller & Pollard, 1977).

Stress inversion methods have been widely used to study the crustal stress in volcano-tectonic settings (Bergerat, 1987; Michael, 1987; Angelier, 1994; Bauve *et al.* 2014; Plateaux *et al.* 2014; Sigmundsson *et al.* 2014) and can be used to recover the past or present-day regional stresses from observed fault and dyke patterns. However, these classic formulations of stress inversion, based on observed fault characteristics, assume that a change of the volumetric stress tensor (i.e. isotropic or hydrostatic stress) has no effect on the fault slip direction and magnitude (*et al.*Angelier, 1979, 1994. 2002; Etchecopar *et al.* 1981; Michael, 1984, 1987). Indeed, such formulations implicitly assume that discontinuities (i.e. faults, magma chambers, salt diapirs, etc.) cannot open or close. In the case of pressurized cavities, however, the effect of the volumetric
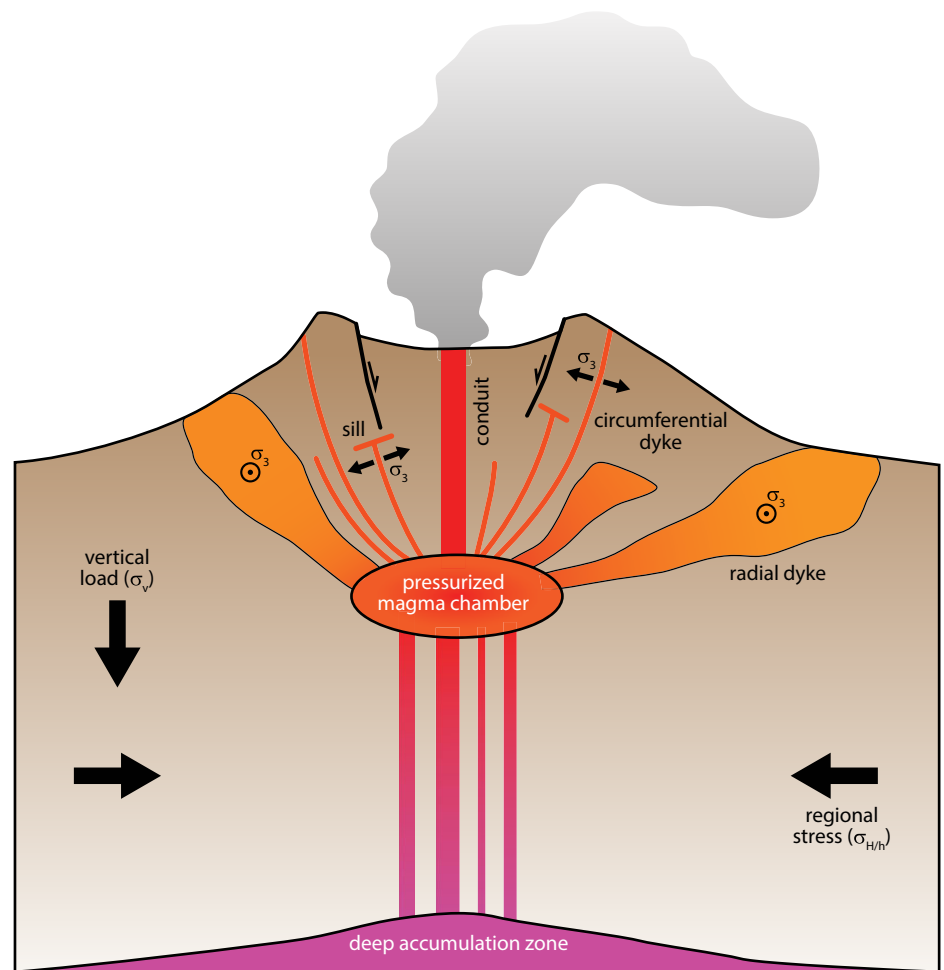
Fig. 1. Schematic illustration of a volcanic edifice and its associated caldera bounded by faults. The deeper accumulation zone feeds the shallower magma chamber through dykes. The magma chamber is the essential component to the volcanic system. Its driving pressure, once exceeding the rock strength, will lead to the initiation and propagation of dykes, not all of which will reach the surface.

part of the stress tensor cannot be neglected as it may affect the resulting displacement (Maerten *et al.* 2018). Muller (1986) and Baer and Reches (1991) have developed interesting inversion methods that take into account volumetric change to recover both the regional stress and magma pressure. They used two-dimensional elastic analytic solutions of a pressurized circular hole subjected to a far field stress as proxy for the magmatic intrusion. Sets of stress trajectories are computed and compared to observed dyke trajectories over a wide range of parameters such as the far field stress magnitude and orientation, the radius of the magma intrusion and its location. While the technique has proven to be efficient, it is nonetheless limited to 2D simulations of circular intrusions.

In this contribution, we combine the efficiency of a linear elastic boundary element method (BEM) with an extended stress inversion formulation (F Maerten *et al.* 2016; L Maerten *et al.* 2016) based on the superposition principle to provide a multiparametric inversion scheme. This inversion takes into account the volumetric change associated with pressurized magma chambers of any 3D shapes and observational data such as observed dyke or eruptive fissure orientations. No attempt is made here to invert for the shape and position of the magma chambers. Instead, we assume geometric 3D shapes and locations based on previous studies.

First, we test the BEM against known analytical solutions and validate that it can be efficiently used to model pressurized cavities. Then we give a detailed description of the inversion methodology. Finally, two well-known study cases located in volcano-tectonic systems are used to test the multiparametric inversion method,

namely the Spanish Peaks and the Galapagos Islands. In both examples, dyke trajectories are the main input to constrain the inversion to yield information on the direction and magnitude of the tectonic stress and internal pressure of magma chambers.

2. Method

The previous conceptual methodology used to recover far field tectonic stresses as well as the magma chamber pressure is to run thousands of simulations covering the range of all possible far field stress configurations and magma pressures. Then, for each simulation, one compares attributes of the modelled stresses with the dyke geometry (i.e. strike and dip) where they are observed. Finally, the simulations that give the best fit between modelled stresses and observed dykes are selected as the optimum models.

This method is based on the following assumptions:

1. Dyke trajectories used to constrain the inversion must have followed the past ambient stresses that are a combination of local stresses near pressurized magma chamber and far field tectonic stresses (Odé, 1957; Muller & Pollard, 1977; Muller, 1986; Baer & Reches, 1991).
2. No other important mechanisms must have constrained the observed dyke propagation paths: for instance, pre-existing fractures or anisotropic materials (e.g. layering) that could deviate dyke paths from the ambient stresses (Jolly & Sanderson, 1995; Gudmundsson, 2011).

2.a. Superposition principle, linear elasticity and BEM

The key idea to efficiently invert for both the tectonic stresses and the pressure in magma chambers while reducing the computation time associated with thousands of simulations is to apply the superposition principle (Brillouin, 1946). This principle states that for any linear system, two or more solutions can be added together so that their weighted sum is also a solution. The use of this principle allows recovery of the displacement, strain and stress anywhere in a model using pre-computed specific values from linearly independent simulations.

In this study we use linear elastic models in our geomechanical simulations to be capable of applying the superposition principle. The use of linear elasticity for modelling deformation and fractures is supported by numerous research studies over the past half-century. These studies have used linear elasticity to effectively explain observed geological structures such as fractures (Kattenhorn *et al.* 2000; Bourne & Willemse, 2001), veins (Soliva *et al.* 2010), dykes (Odé, 1957; Muller & Pollard, 1977; Baer & Reches, 1991), fault slip (Maerten, 2000), fault-related deformation (Maerten *et al.* 2000) and even salt-related deformation (Luo *et al.* 2012). We therefore believe that such mechanical elastic behaviour is appropriate as a first approximation for modelling dyke propagation from magma chambers or stocks.

Several 3D numerical methods can be used with this methodology, such as the finite element method (FEM), the finite difference method (FDM) or the boundary element method (BEM). We decided to adopt the BEM because it has already proven to be useful for far field stress inversion (Kaven *et al.* 2011; F Maerten *et al.* 2016). In addition, it has a feature that is better suited for the proposed multiparametric inversion method: only the 3D surfaces representing displacement discontinuities such as fractures, cavities, intrusions and bedding interfaces have to be defined as triangulated surfaces while the volume of the model does not have to be built and meshed explicitly.

We have therefore developed and used a BEM called ARCH, which has the same foundations as Poly3D (Thomas, 1993; Maerten *et al.* 2005) and iBem3D (Maerten *et al.* 2014), except that it has been optimized and it incorporates the singularity corrections identified by Nikkhoo and Walter (2015). In the proposed method we assume that a magma chamber or a stock can be compared to a pressurized cavity with prescribed traction boundary conditions. Therefore, to validate that the BEM numerical technique can model pressurized cavities, we benchmarked this method against the closed form solution of a pressurized cylindrical body subjected to a 3D far field stress (Fjaer *et al.* 2008). This solution allows computing the stress at a given point around a pressurized cylindrical cavity (see Supplementary Material 1, available online at https://doi.org/10.1017/S001675682200067X). The BEM approach validates against the known analytical 3D solution of a pressurized cylinder subjected to a 3D far field stress, showing a perfect agreement between the two solutions.

2.b. Definition of the parameter space

The three main unknowns for geomechanically studying volcanoes and their associated deformation are (1) the magma chamber geometry, (2) the far field tectonic stresses and (3) the magma density and excess pressure. In this contribution, we did not invert for the shape and position of the magma chambers, but instead used simple assumptions based on previous work. In the following

section, we therefore exclusively concentrate on unknowns (2) and (3) and define all the associated parameters that we called the parameter space.

2.b.1. Far field stress and local boundary conditions

In most previous stress inversion techniques (*et al.*Kaven *et al.* 2011; Célérier *et al.* 2012; F Maerten *et al.* 2016), the stress ratio (Angelier, 1979) is solely used to describe the change in shape of the stress ellipsoid. These inversion techniques are implicitly based on the hypothesis that fault walls are constrained to slip without the possibility to overlap or open. This is schematically illustrated in 2D in Figure 2a, b, where a faulted block will slide in response to either (i) a vertical compression (Fig. 2a) or (ii) a horizontal tension (Fig. 2b). If we assume that the fault walls cannot open or overlap, (i) and (ii) are equivalent and the notion of stress ratio can be introduced within the far field stress tensor as a unique parameter.

In three dimensions, the regional stress is written as follow:

$$
\sigma_R = Q \begin{bmatrix} \sigma_1 - p_p & & \\ & \sigma_2 - p_p & \\ & & \sigma_3 - p_p \end{bmatrix} Q^T = (\sigma_1 - \sigma_3) \, Q \begin{bmatrix} 1 & & \\ & R & \\ & & 0 \end{bmatrix} Q^T
$$
$$
- (p_p - \sigma_3) I_3 \equiv Q \begin{bmatrix} 1 & & \\ & R & \\ & & 0 \end{bmatrix} Q^T
$$
(1)

where $R = (\sigma_2 - \sigma_3)/(\sigma_1 - \sigma_3)$ is the stress ratio, Q is the 3D rotation matrix containing the three Euler angles (φ, θ, ψ), and p_p the pore pressure. As previously mentioned, the first simplification in Equation 1 comes from the fact that the isotropic part of the stress tensor, $(p_p - \sigma_3)I_3$, will not influence the fault slip direction and magnitude. Therefore, only the deviatoric part contributes to the shear stress since the isotropic pressure part results in a force normal to any plane. Similarly, the scaling coefficient given by the maximum differential stress, $(\sigma_1 - \sigma_3)$, only affects the fault slip magnitudes, not the directions. Therefore, it is discarded as a second simplification.

However, if we allow either opening or overlapping of the discontinuity walls with a displacement perpendicular to the walls (e.g. a change in volume), the resulting displacements and stress fields are substantially different. The most common opening-mode discontinuities in nature are the joints, veins (tension gashes) and dykes but they also include inflating magma chambers, salt bodies or cavities caused by increased pressure. The most typical natural overlapping mode discontinuities are compaction bands and dissolution seams (stylolites) but they also include deflating magma chambers, salt bodies or cavities caused by a decreased internal pressure.

To better illustrate this effect, we performed a 3D numerical model of the cases presented in Fig. 2, representing an inclined fault subjected to a uniaxial tension or compression in the *x*–*y* plane. In Figure 3a, b, the fault is subjected to a traction boundary condition in the fault plane such that it is free to slip, and has imposed zero displacement in the normal direction to the fault plane to prevent any opening or overlapping of the fault walls. In such a configuration, applying a compression along the *y*-axis (Fig. 3a) or a tension along the *x*-axis (Fig. 3b) gives similar contours of the displacement norm around the fault. In contrast, in Figure 3c, d the fault is subjected to traction boundary conditions in all three local directions (both perpendicular and parallel to the

Fig. 2. A 2D faulted block with normal slip which can be the result of (a) a vertical compressive stress or (b) a horizontal tensile stress. In both cases, one must assume that the fault walls cannot overlap or open. When overlapping or opening is allowed, the result of a vertical compression (c) or a horizontal tension (d) is fundamentally different from (a) and (b).
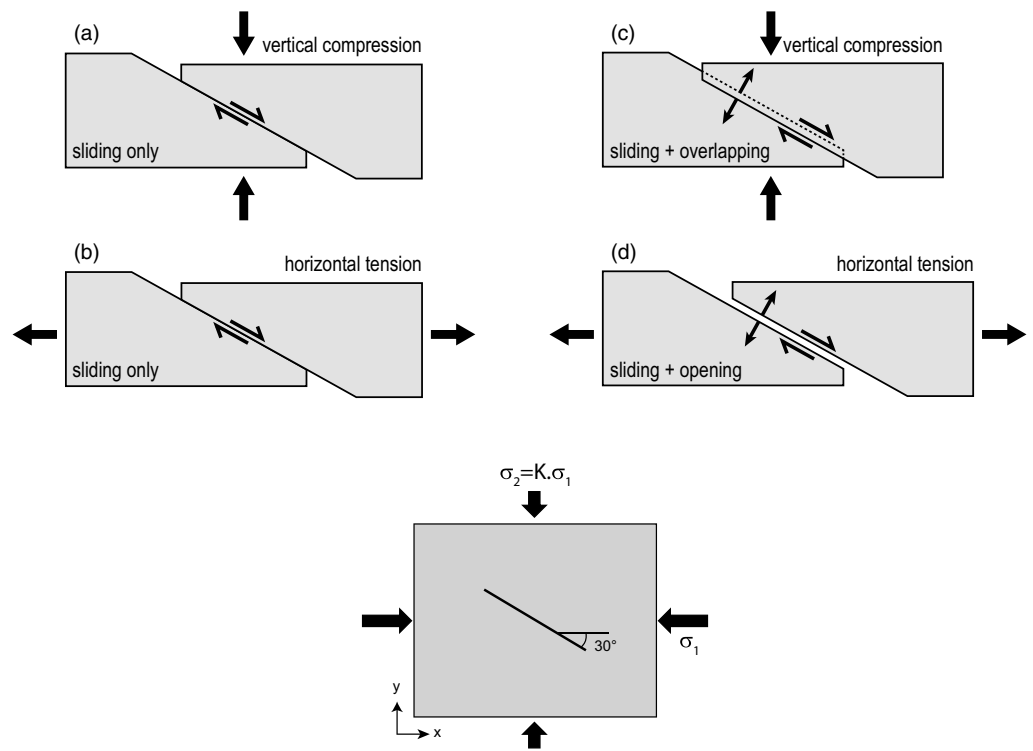

Fig. 3. Effect of fault slip on the predicted displacement field norm using uniaxial remote loadings. The predicted results give similar iso-contours when shearing is only permitted with uniaxial compression (a) or tension (b). In contrast, the predicted results give different iso-contours when opening or overlapping of the fault walls is permitted with uniaxial compression (c) or tension (d).
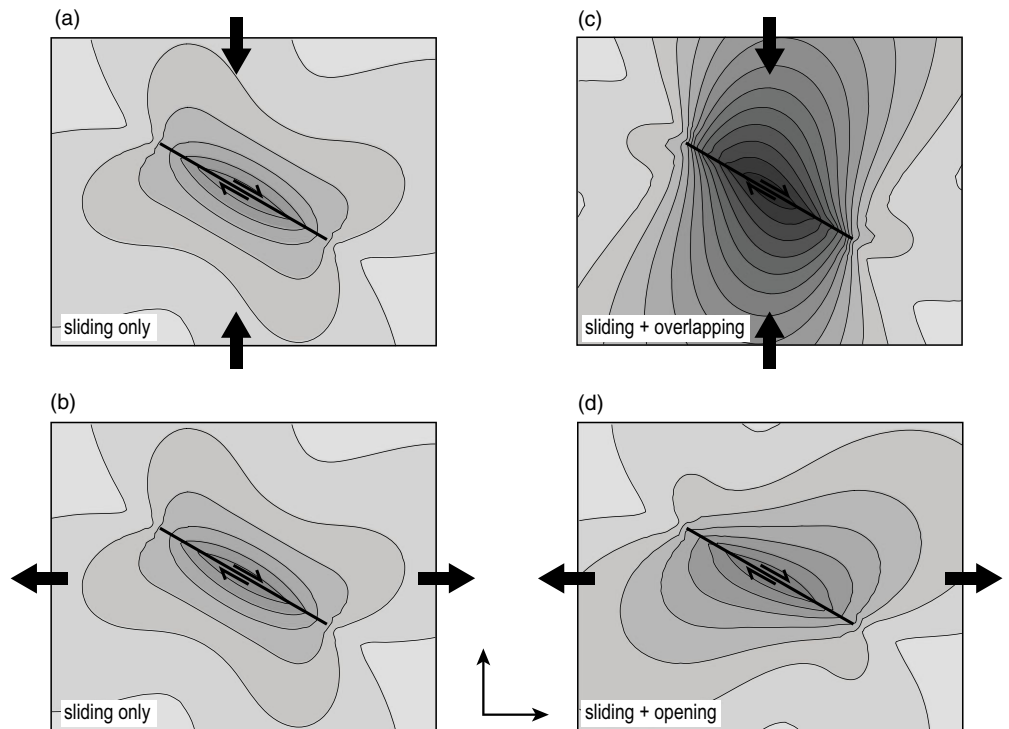
fault plane). Consequently, the fault walls are still free to shear, but also free to overlap or open. Applying a compression (Fig. 3c) or a tension (Fig. 3d) now gives different results in terms of normalized displacement fields compared to Figure 3a, b.

In Maerten *et al.* (2018), a similar conclusion was presented using modelled σ_1 trajectories, and that was compared with experiments done in PMMA (polymethyl methacrylate) containing open

defects subjected to compression (de Joussineau *et al.* 2003). By allowing overlapping or opening of fault walls, a vertical compression or a horizontal tension leads to different results (Figs 2c, 3c and 2d, 3d, respectively). This is also demonstrated in Jaeger *et al.* (2009: 249–50) where the stress distribution along the edge of a penny-shaped crack subjected to shear and/or opening is analytically formulated (i.e. equations 8.313–8.323). These equations

demonstrate that adding opening or interpenetration during shearing gives different results than when modelling shearing only.

Consequently, the reduced stress tensor cannot be used solely for modelling pressurized discontinuities as we must impose traction boundary conditions in the normal direction of discontinuities, which in turn implies a potential change in volume. Equation 1 is rewritten accordingly

$$\sigma_R = (\sigma_1 - \sigma_3) \left(Q \begin{bmatrix} 1 & & \\ & R_s & \\ & & 0 \end{bmatrix} Q^T - R_v I_3 \right) \quad (2)$$

in which

$$\begin{cases} R_s = (\sigma_2 - \sigma_3)/(\sigma_1 - \sigma_3) \\ R_v = (p_p - \sigma_3)/(\sigma_1 - \sigma_3) \end{cases} \quad (3)$$

In addition to $R \in [0, 1]$, which we rename R_s with the subscript '*s*'for shear, we define the stress ratio $R_v \in \mathbb{R}$ for which the subscript '*v*' stands for volumetric. The parameter space extends from $\sigma_R(\varphi, \theta, \psi, R_s)$ to $\sigma_R(\varphi, \theta, \psi, R_s, R_v)$, with φ, θ, ψ the three Euler angles.

2.b.2. Magma pressure

We now further define the total pressure (p_m) inside a magma chamber as

$$p_m(z) = p_e + \rho_m g |z| = p_e + p(z) \quad (4)$$

where p_e represents the excess pressure, i.e. the pressure of the chamber at depth $z = 0$, and $p(z)$ the isotropic magma pressure with ρ_m being the density of the magma in the chamber. We assume that the pressure can take any positive value (i.e. excess pressure) or negative value (i.e. deficient pressure). The total magma pressure, p_m, is consequently the general formulation incorporating the excess pressure (Yun *et al.* 2006; Gudmundsson, 2012), the isotropic magma pressure and the effect of the density contrast inside a magma chamber.

2.c. Applying the superposition principle

Our goal is then to estimate, through the multiparametric inversion, the parameters p_e and ρ_m (if not imposed), in addition to the far field stress parameters, $\sigma_R(\varphi, \theta, \psi, R_s, R_v)$.

As stated above, using the principle of superposition, it is possible, given a number of linearly independent solutions of a model, to compute the solution for a change in pressure in a magma chamber, a change in magma or rock density, a change of the Young's modulus or a change in the far field stress. To this end, the input parameters $(\varphi, \theta, \psi, R_s, R_v, \rho_m, p_e)$ are transformed into linear parameters (F Maerten *et al.* 2016)

$$S = \{\sigma_R, \rho_m, p_e\}^T = \{\sigma_{xx}, \sigma_{xy}, \sigma_{xz}, \sigma_{yy}, \sigma_{yz}, \sigma_{zz}, \rho_m, p_e\}^T \quad (5)$$

These constitute the eight independent simulations that must be performed for the inversion of the regional stresses and the excess pressure of one magma chamber. In Equation 5, σ_R represents the components of the far field stress in the global coordinate system. Given eight initial linearly independent simulations, any far field stress, excess pressure and magma density can be written as a linear combination of these eight initial simulations:

$$\{\sigma_R, \rho_m, p_e\}^T = S = [S_1 \dots S_8] \begin{Bmatrix} \alpha_1 \\ \vdots \\ \alpha_8 \end{Bmatrix} = A\alpha \quad (6)$$

where each S_i represents a column of a matrix A, i.e. different linearly independent boundary conditions and model parameters applied to the model (far field stress, excess pressure and magma density) for the initial simulations. By linearly independent simulations, we mean that a simulation cannot be written as a linear combination of other simulations. In other words, the equation $\sum_{i=1}^{8} \alpha_i S_i = 0$ can only be satisfied when $\alpha_i = 0$ for $i \in [1, 8]$. As described in F Maerten *et al.* (2016), the simplest and most stable way (in term of matrix condition) to choose the linearly independent remote stresses, magma density and excess pressure is such that A is the identity matrix, constituting the natural basis vectors of dimension eight. In that case, Equation 6 simplifies to $S = \alpha$, and parameter α represents both the linear coefficients for the superposition and the physical parameters

$$\alpha = \{\sigma_{xx}, \sigma_{xy}, \sigma_{xz}, \sigma_{yy}, \sigma_{yz}, \sigma_{zz}, \rho_m, p_e\} \quad (7)$$

If at a given observation point, P, in the three-dimensional space, we store the total stress (i.e. the perturbed stress caused by pressurized magma chambers and any sliding faults, plus the far field stress) for the eight simulations, σ_P^i, then the total stress at P for a given α is simply $\sigma_P = \sum_i \alpha_i \sigma_P^i$. When a gradient is used for the far field stress and pressures, then all the initial simulations must be performed using the gradient as well.

The superposition algorithm is summarized in Supplementary Material 2 and the case of multiple pressure inversion is described in Supplementary Material 3 (both available online at https://doi.org/10.1017/S001675682200067X).

In the following case studies, we have reduced the parameter space as follows. We assume that the magma density is known ($\rho_m = 2600$ kg m^{-3}). Therefore, ρ_m is fixed in the parameter space. Then we assume that one of the principal stress directions is vertical (Anderson, 1905; Lisle *et al.* 2006). Therefore, depending on which of the principal stresses is vertical, we can cover the normal, strike-slip and reverse fault stress regimes with $\sigma_v = \sigma_1$, $\sigma_v = \sigma_2$ and $\sigma_v = \sigma_3$ respectively. This assumption implies that $\sigma_{xz} = \sigma_{yz} = 0$ from the parameter space.

2.d. Inversion strategy and objective functions

As in F Maerten *et al.* (2016) and L Maerten *et al.* (2016), multiple types of weighted data can be used and combined to constrain the multiparametric inversion, under the condition that an objective function can be defined for each data type. Examples of such data are focal mechanisms (F Maerten *et al.* 2016), fractures (L Maerten *et al.* 2016), dykes or eruptive fissure orientations, interferometric synthetic aperture radar (InSAR), GPS, tiltmeter or microseismicity measurements (Maerten, 2010a).

Then any search algorithm can be used to determine the best parameters (i.e. α) that minimize the objective functions. For instance, in F Maerten *et al.* (2016) and L Maerten (2016), a Monte Carlo approach was used where the parameter space was sampled randomly and the solution, which minimized the objective functions, was retained. Other search algorithms can be used such as the Bee (Pham *et al.* 2005) or the Ant (Dorigo, 1992) algorithms. It is worth mentioning that if a parameter is known, then the corresponding α_i is set accordingly and kept fixed while using a search

algorithm. Similarly, unknown α_i can be bounded in the parameter space if necessary.

In the following case studies, we define the objective function for a dyke located at P_i such that the computed local minimum principal direction of the perturbed stress (geologist convention), σ_3, is aligned with the normal n direction, perpendicular to the observed dyke

$$f_i = \frac{2w_i}{\pi} \cos^{-1} |\sigma_3 . n| \qquad (8)$$

In Equation 8, w_i represents the weight of the dyke and '.' represents the dot product. The absolute value is taken since the normal can be defined on either side of the dyke. This objective function is zero when σ_3 is collinear with n. When using dyke traces, the z component of both σ_3 and n is set to zero (i.e. projected onto a horizontal plane) and the two vectors are normalized before using Equation 8.

3. Case studies

We have chosen two natural examples of magma intrusion at volcanoes that are known to display associated dykes for which the propagation path is believed to be affected by both local and regional stress fields. Our goal is to use these two examples as a proof of concept of the method described above. We do not discuss in any depth the geological evolution of these two case studies.

3.a. Spanish Peaks

The Spanish Peaks area is located in south-central Colorado, USA (Fig. 4), and is famous for its well-exposed radial dyke system. The two prominent topographic features composed of igneous, metamorphosed and deformed sedimentary rocks are the West and East Spanish Peaks. The peak intrusions, often referred as stocks (Johnson, 1961), were emplaced during late Oligocene to early Miocene time (Armstrong, 1969; Stormer, 1972; Smith, 1975, 1978). Rocks of both peaks and the surrounding dykes produced the remarkable relief when exhumed due to regional uplift and erosion, being more resistant to weathering than the surrounding sedimentary rocks.

The numerous sub-vertical dykes that crop out around the peaks were first described by Hills (1901) and originally mapped out by Knopf (1936). They vary from 1 to 30 m in thickness and are exposed for distances of up to 20 km. The dykes are divided into three distinct groups: independent, subparallel and radial dykes (Johnson, 1968). The radial dykes are syenite and syenodiorite and are focused approximately on West Spanish Peak (Fig. 4).

Since its first description, the radial dyke pattern at Spanish Peaks has been the subject of several hypotheses regarding its genesis and development. Hills (1901) supposed that dykes adjacent to the West Spanish Peak filled radial fractures formed during doming of the sedimentary rocks by the emplacement of the stocks. Knopf (1936) thought that the possible 'cause for this swinging around to an east–west direction is that the forces that, near the stocks, produced the radial fissuring, opened up, at a greater distance from the stocks, the latent tension fissures produced during the compression that had folded the sedimentary beds into a broad syncline before the stocks were injected, *i.e.* the dykes availed themselves of latent tension breaks across the axis of the fold'. Following Knopf's idea, Johnson (1961) argued that selective magma intrusion into pre-existing complex fracture sets could

have accounted for the observed dyke patterns. These fracture sets could be the result of successive orogenic stresses of varying direction and magnitude during folding of the syncline before intrusion of the stocks. In Odé (1957), the similarity between the Spanish Peaks radial dyke pattern and the pattern of maximum principal stress trajectories for a particular elastic model was noted and an explanation that relates the dyke pattern to a model stress field was proposed. It is based on Anderson's (1951) postulate that dykes follow trajectories normal to the direction of the least principal stress. Odé's work suggests that the stress trajectories were mainly controlled by the stock, the Sangre de Cristo Range to the West, as well as the maximum principal regional stress orientation. Therefore, his model consisted of a pressurized circular hole – the West Spanish Peak stock – adjacent to a rigid, planar boundary – the Sangre de Cristo Range to the west – in a 2D elastic plate. On this stress system he superimposed a homogeneous far field stress having principal stresses parallel and perpendicular to the rigid boundary. The far field stresses simulated the regional stress state in the horizontal plane at the time of intrusion. Muller and Pollard (1977) and Muller (1986) further explored Odé's model by adding a far field oblique stress to the Sangre de Cristo Range rigid boundary, producing stress trajectories that mimic the dyke pattern remarkably well.

3.a.1. Spanish Peaks model configuration

Here, we adopt Odé's stress hypothesis, and we apply the multiparametric inversion technique described above to the Spanish Peaks radial dyke pattern to find the optimum mechanical parameters when the magma intrusion and dykes were emplaced: (1) the magma pressure, (2) the orientation of the maximum horizontal far field stress and (3) the relative magnitude of the two far field horizontal stresses.

While our geomechanical simulations are in 3D, we nonetheless model the West Spanish Peak stock as a vertical cylindrical body (Fig. 5a) in a whole elastic space (Muller & Pollard, 1977) that is equivalent to a 2D model, where the vertical cylindrical body is long enough to reduce the upper and lower edge effects. The modelled stock radius is 1.4 km, instead of the 2.6 km used by Muller and Pollard (1977), to prevent the observed dykes from being inside the modelled stock (Fig. 5b). No other geological information is available to constrain the idealized stock geometry.

We used a value of 0.25 for Poisson's ratio (ν) and 30 GPa for Young's Modulus (E), which are the mean values representative for sediments.

In this pseudo-2D mechanical simulation the vertical far field stress has no effect on the results. The Andersonian 3D far field stress is defined by the two horizontal stresses that are normalized with respect to σ_v such that $k_H = \frac{\sigma_H}{\sigma_v}$ and $k_h = \frac{\sigma_h}{\sigma_v}$. Therefore, the modelled far field stress consists of the relative magnitudes of the two horizontal stresses, σ_H and σ_h, as well as the orientation (θ) of σ_H with respect to north. In our simulations, these far field stress parameters are unknowns of the multiparametric inversion process.

To simulate the magma pressure, a traction component normal to the cylinder surface ($P_m(z)$) is initially set to allow inflation (i.e. positive traction) or deflation (i.e. negative traction) in response to both the imposed $P_m(z)$ and the far field stress. The two other initial traction components, parallel to the stock surface, are set to zero. In our simulations, we normalize the magma pressure with respect to σ_v such that $k_p = \frac{P_m(z)}{\sigma_v}$. The ratio k_p is therefore another unknown of the multiparametric inversion process.
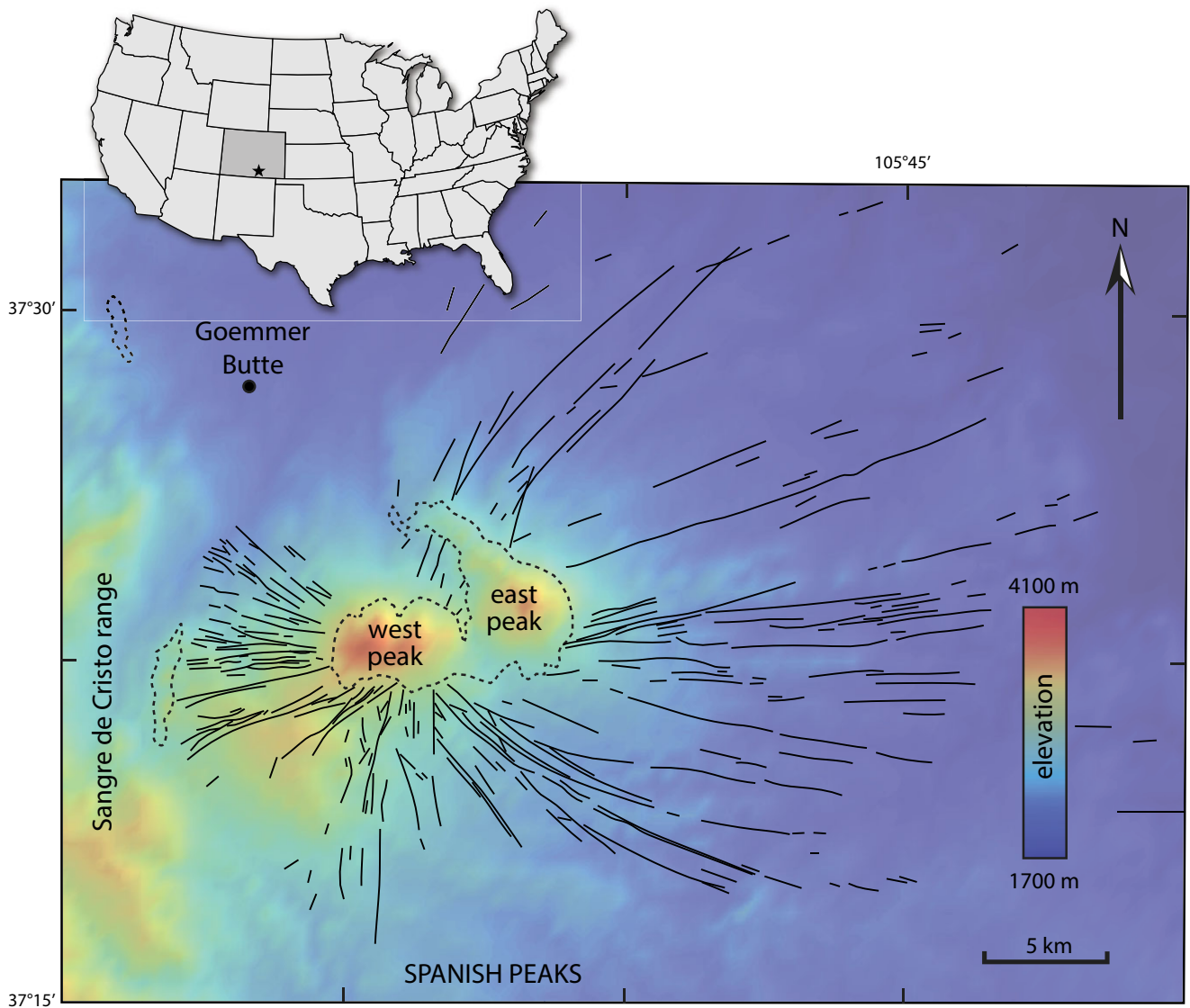
Fig. 4. Map of syenite and syenodiorite dykes (solid lines) in the Spanish Peaks region of south-central Colorado (USA) from Johnson (1968) over topography (coloured by elevation). Closed dashed lines are the boundaries of igneous intrusive rock (the Spanish Peaks stock).
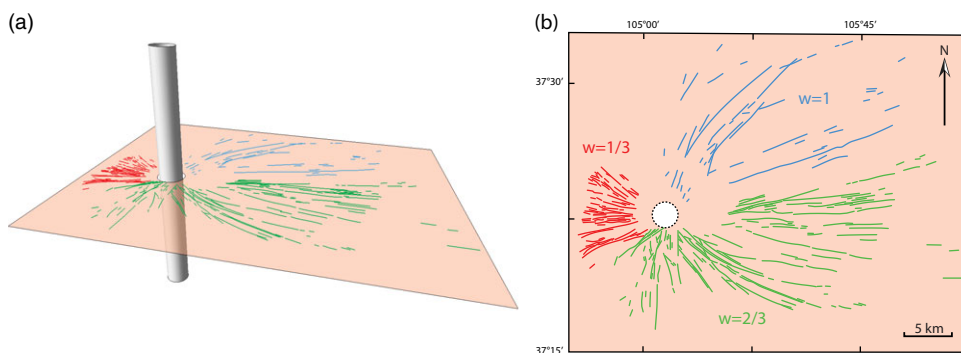

Fig. 5. Spanish Peaks model configuration. (a) 3D view of the vertical cylinder with a radius of 1.4 km used to model the west Spanish Peaks stock. (b) Map view of observed dykes colour-coded with respect to the weight (w) used to constrain the multiparametric inversion.

In contrast to the models from Odé (1957) and Muller and Pollard (1977), we did not attempt to model the effect of the Sangre de Cristo Range rigid boundary to the west.

The inversion process is constrained by the mapped subvertical dykes (Fig. 4) along with their known dip angle (~90°)

and azimuths. The dykes are placed at the mid-height of the vertical cylinder. The objective function used for the simulation is that described earlier for dykes.

Since this multiparametric inversion is solely constrained by the location, the dip and strike of the observed dykes, it is important to

consider the fact that dykes are not necessarily evenly distributed or observed in the area (Fig. 4). This could have a significant effect on the far field stress inversion outcome as, for instance, a large concentration of radial dykes near the stock will downplay the effect of few curving dykes in the distance, which better indicate the regional stress orientation. We therefore decided not to give equal weight to each datum to account for the observed uneven dyke density. As illustrated in Fig.5b, the closely spaced western dykes in red observed between the cylinder and the Sangre de Cristo Range have a weight of 1/3, the southern dykes in green have a higher weight of 2/3 and the sparsely spaced northern dykes in blue have the highest weight of 1.

A horizontal observation grid, covering the entire study area, was placed at the mid-height of the vertical stock. A set of observation points, where we modelled potential dyke orientations derived from the computed perturbed stress field, are used to compare with the observed dyke patterns.

3.a.2. Spanish Peaks inversion results

To better visualize and analyse the results of the multiparametric inversion, we use a modified domain introduced by Muller (1986). This domain consists of a half-circular graph (Fig. 6e) for which the radius is the ratio defined as k_h/k_H which goes from 1 to 0 and the angular coordinate defines the orientation (θ) of the maximum horizontal stress relative to north from 0° to 180°. Because the inversion was done for three parameters ($\frac{k_h}{k_H}$, k_p and θ), we deliberately fixed k_p to the optimum value found and only plot k_h/k_H versus θ. A point in the domain represents a single simulation; each simulation is coloured according to the mean misfit angle ($\bar{\delta}$) which is the arithmetic mean of all the misfit angles (δ) for all dykes. δ is the angle between the observed dyke strike direction, d_o, and the modelled dyke strike direction, d_m, which varies from 0° to 90°, 0° being the best fit and 90° being the worst.

It is defined as

$$\delta = \frac{180}{\pi} \cos^{-1} |d_0.d_m| \qquad (9)$$

The multiparametric inversion, which consists of six linearly independent forward simulations and 30 000 random geomechanical simulations, was run in less than 1 min (see Supplementary Material 4, available online at https://doi.org/10.1017/S001675682200067X). The optimum solution was found for a relative magma pressure k_p =1.67, a far field maximum horizontal stress (σ_H) oriented N81.2°E and a horizontal stress ratio $\frac{k_h}{k_H} = 0.76$, for a mean misfit angle $\bar{\delta} = 4.6°$. This result is highlighted in the multiparametric inversion domain with the green colours (black circle in Fig. 6e). Figure 6a shows a qualitative comparison between the observed dyke pattern and the modelled dyke trajectories derived from the stress field. Since dykes (i.e. opening-mode fractures) propagate in a plane normal to the local direction of the least compressive stress (i.e. σ_3), the streamlines shown in Figure 6a represent the strike of the planes containing σ_1 and σ_2, which are mostly sub-vertical in this case. The modelled dyke trajectories show a good correspondence with the observed dyke pattern. Near the stock, the dyke trajectories converge to form a radial pattern but become more parallel to the far field stress, $\sigma_H = $ N81.2°E, at a greater distance (i.e. 20 km). The modelled dyke trajectories show one of the two unique points where their orientation is not defined (orange dot in Fig. 6a). These are referred to as isotropic stress points where $\sigma_h = \sigma_H$. This point, located to the

north, does not fall at the Goemmer Butte (Fig. 4) as in the Muller and Pollard (1977) model because the rigid boundary effect of the Sangre de Cristo Range has not been taken into account.

3.a.3. Sensitivity to far field stress characteristics

We also evaluated the extent to which the modelled stress trajectories, hence the spatial distribution of the dykes around the West Spanish Peak stock, are sensitive to the far field stress characteristics. We arbitrarily chose a different but realistic far field state of stress (the 'non-optimal' results shown in Fig. 6b, d) for which σ_H is oriented N30°E and the horizontal stress ratio $\frac{k_h}{k_H} = 0.4$. This is shown as a white circle in the multiparametric inversion domain of Figure 6e. The relative pressure k_p inside the stock is the same as for the previous model.

This model configuration gives a mean misfit angle $\bar{\delta} = 14.1°$, which is almost three times higher than for the optimum model configuration. The histograms of the misfit angles, computed at each dyke segment for the two model configurations, are shown in Figure 6c, d. The general shape of the histograms is a good indicator of the goodness of fit: a flat histogram means that the fit is poor, whereas rapid decay with increasing misfit angle, as shown in the optimum model parameters of Figure 6c, means that the model fit is much better. Furthermore, the histogram of the optimum model parameters shows that 89.6 % of the observed dykes have a misfit angle less than 10°, whereas it is only 49.9 % for the non-optimum model.

Figure 6b illustrates a comparison between the non-optimum modelled dyke orientations and the observed dyke pattern. Again, the non-optimum modelled stress trajectories near the stock converge to radial, but at *c.* 10 km from the stock the modelled dyke trajectories become parallel to the far field stress (N30° E), and deviate from the observed dyke trajectories.

3.b. Galapagos Islands

The Galapagos archipelago is located at *c.* 1000 km west of Ecuador. It is a group of volcanic islands that are the product of a fixed oceanic hot spot under the Nazca plate. The formation of the Galapagos Islands is estimated at 3.9 Ma ago (Geist *et al.* 1986). Due to the eastward motion of the Nazca plate, volcanoes are progressively younger and more active towards the west and the activity of the hot spot is now centred at Isabela and Fernandina islands (Fig. 7). In this case study, the seven active volcanoes of Isabela and Fernandina islands are considered for simulation, namely Fernandina, Ecuador, Wolf, Darwin, Alcedo, Sierra Negra and Cerro Azul volcanoes.

These basaltic shield volcanoes with large summit calderas are characterized by numerous linear eruptive fissures (Chadwick & Howard, 1991), which are the result of dykes propagating from magma chambers beneath the calderas and intersecting the surface. These fissures (and their underlying dykes) display a very distinctive pattern that is circumferential around the calderas and radial on the flanks of the volcanoes (Fig. 7). This pattern of circumferential and radial dykes is intriguing because it is poorly documented on other basaltic shield volcanoes.

The longest eruptive fissure is *c.* 2.6 km, while the average is 0.6 km long. The radial eruptive fissures tend to concentrate between adjacent Galapagos volcanoes and diverge slightly to display a continuous pattern between volcanoes, suggesting coeval development (Fig. 7). This pattern is expected from the stress field interaction from two or more sources of pressurized magmatic chambers modified to some extent by regional
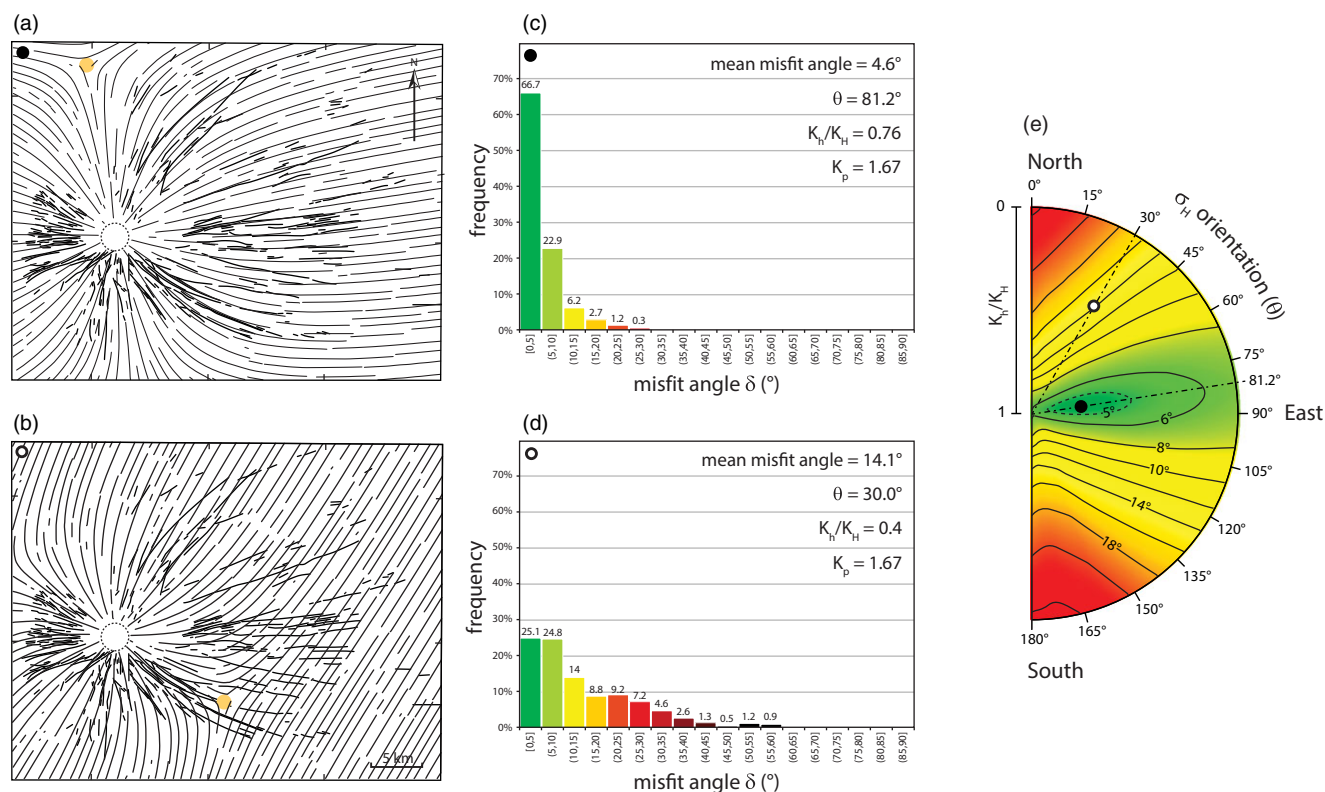
Fig. 6. Spanish Peaks model results. (a, b) Maps of observed dykes and modelled dyke trajectories for the optimum and example non-optimum model parameters respectively. Orange circles highlight the location of computed isotropic stresses where dyke trajectories cannot be defined. (c, d) Histograms of the misfit angles (δ) for the optimum and non-optimum model parameters, respectively. (e) Multiparametric inversion domain showing the location of the optimum (black circle) and non-optimum (white circle) models. The colour scale and contours show the mean misfit angle ($\bar{\delta}$).

stresses (Chadwick & Dieterich, 1995). The radial eruptive fissure pattern observed in the Galapagos islands is somewhat similar to that in models used to explain dyke patterns at Spanish Peaks (Fig. 4).

The circumferential eruptive fissures in the Galapagos Islands are located within 1.5 km of caldera rims. They have often been interpreted as a direct consequence of the caldera faults channelling the magma to the surface (Nordlie, 1973; Browning & Gudmundsson, 2015) or as dyke propagation within a radially oriented stress field in the summit regions due to the steep topography of the caldera walls (Munro & Rowland, 1996). However, according to Chadwick and Howard (1991) 'the circumferential fissures are not simply leaky faults, but their underlying dykes are emplaced as distinct and independent structures and require a specific stress field suitable for the observed fissure orientations'. Also, according to the same authors, the circumferential and radial eruptive fissures appear to have grown contemporaneously and are coexistent. Their interpretation is supported by the fact that (i) both circumferential and radial eruptions have occurred on individual Galapagos volcanoes in historical time, (ii) some individual eruptive fissures have a circumferential orientation near the caldera and gradually curve downslope to become radial and (iii) all fissures erupt the same tholeiite basalt (McBirney & Williams, 1969).

Other hypotheses have been developed to account for the contemporaneous development of both circumferential and radial eruptive fissures: (i) stress perturbations due to a pressurized magma chamber (Chadwick & Dieterich, 1995; Bistacchi *et al.* 2012; Chestler & Grosfils, 2013), (ii) stress perturbation caused by the gravitational unloading due to surface mass redistribution

associated with the formation of a caldera (Corbi *et al.* 2015) and (iii) stress related to the loading of the volcanic edifice (Maccaferri *et al.* 2011; Rivalta *et al.* 2015) by lava flow emplacement.

3.b.1 Galapagos model configuration

We are adopting the hypotheses that dykes will follow the ambient heterogeneous stress field produced by both the magma chamber pressurization and the regional stresses. As suggested by Pollard (1987), it is not necessary that fractures occur before any dyking can take place, because dykes can create their own fractures which propagate immediately ahead of the advancing magma. We therefore apply the multiparametric inversion method described above to the Galapagos Islands dyke pattern to find the optimum mechanical parameters including: (1) the magma chamber pressure for each volcano, (2) the orientation of the maximum horizontal far field stress and (3) the magnitude of the two far field horizontal stresses and the stress regime.

The 3D model of the seven shallow magma chambers was built with oblate ellipsoids for which the horizontal dimensions (long and short axis) and their orientation are derived from the caldera shape of each volcano (Fig. 8). Their dimensions are reported in Table 1. The ratio of the longest axis over the vertical axis is the same for all magma chambers and set to 3.9. The depth of all magma chamber tops is fixed to 2000 m below sea level. These configurations, inspired by previous modelling work from several authors (Chadwick & Dieterich, 1995; Yun *et al.* 2006; Chestler & Grosfils, 2013; Corbi *et al.* 2015), are probably not optimum shapes but they had to be defined for the inversion.
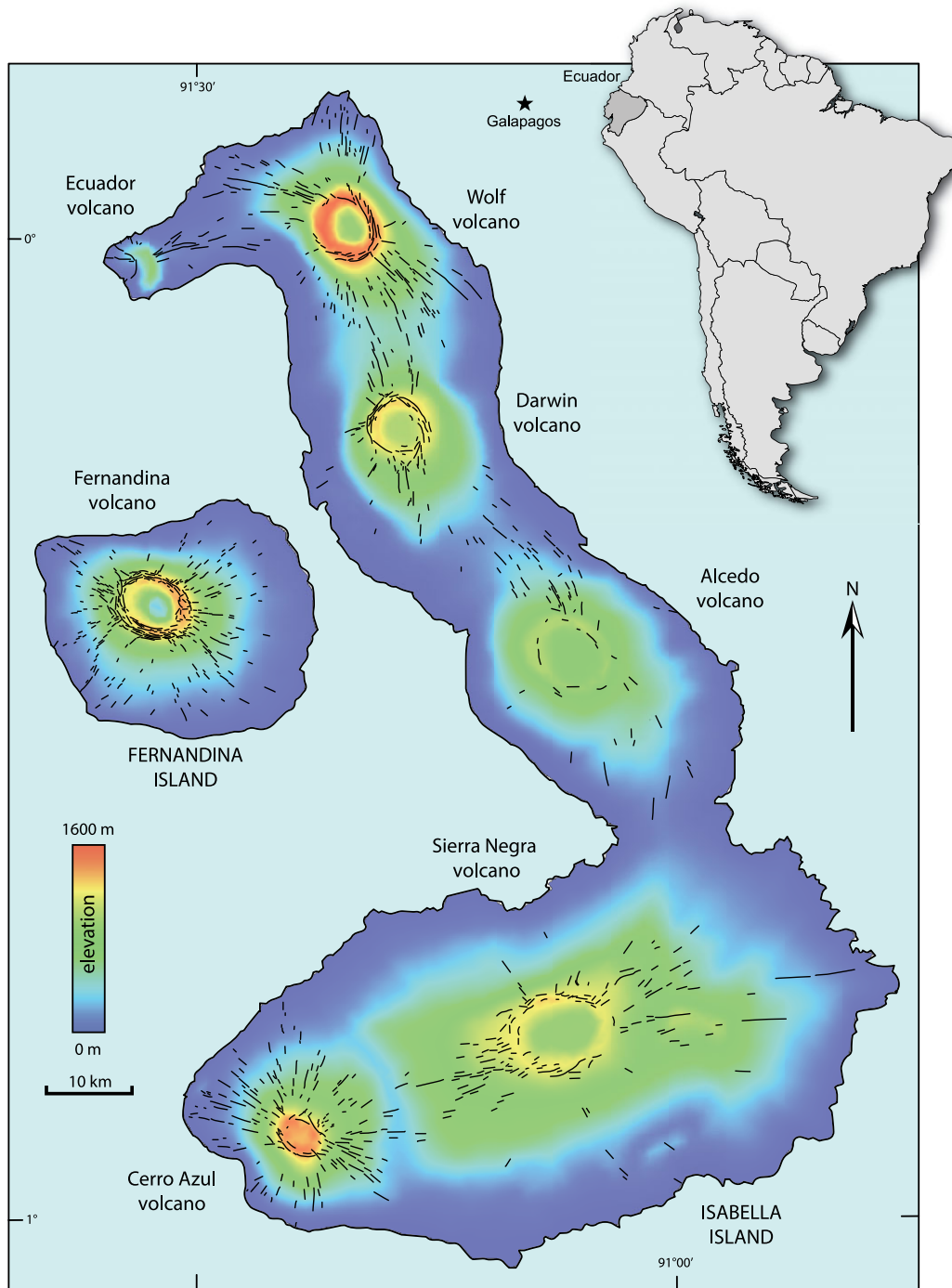
Fig. 7. Map of the eruptive fissures (solid lines) on Fernandina and Isabela islands of the Galapagos archipelago (Ecuador) over topography (colour scale). Modified from Chadwick and Howard (1991).

To simulate the magma pressure, a traction component normal to the magma chamber internal surface ($P_m(z)$) is initially set. In contrast to the Spanish Peaks simulation, stress and pressure gradients are accounted for. The pressure applied on the chamber surfaces is the isotropic pressure of the magma ($\rho_m g|z|$) plus or minus a constant pressure (p_e) depending on whether we model an inflating or a deflating chamber respectively and where ρ_m is the magma density ($\rho_m = 2600$ kg m^{-3}), g is the gravitational

constant and z is the depth. The two other traction components, parallel to the chamber surfaces, are set to have initial tractions equal to 0. In our simulations, p_e is one of the unknowns of the multiparametric inversion process. However, since there are seven magma chambers, there is one p_e per chamber, which makes seven unknowns instead of one in the Spanish Peaks model above.

The Andersonian 3D far field stress is defined such that σ_v is vertical compressive stress related to the overburden load such that
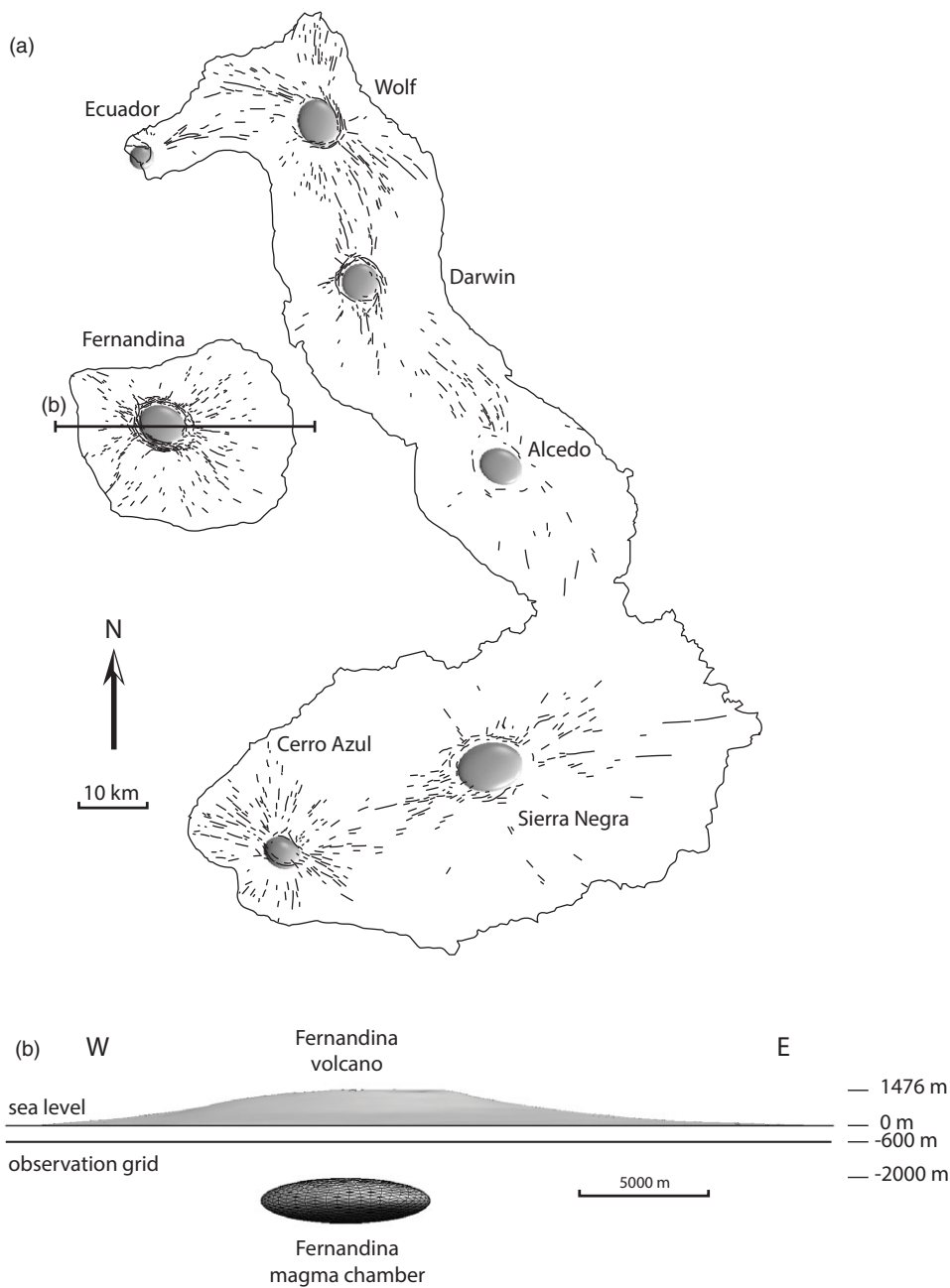
Fig. 8. Ellipsoid geometry of the modelled seven magma chambers. (a) Top view of the magma chambers and their respective locations with the observed eruptive fissures (black lines) used to constrain the multiparametric inversion. (b) Side view from the south of the Fernandina volcano and its modelled magma chamber. The 2D observation plane is placed at 600 m below sea level.

$\sigma_v = \rho_{rock} gz$, where ρ_{rock} is the mean rock density ($\rho_{rock} = 2900$ kg m^{-3}) and k_H and k_h are defined as $k_H = \frac{\sigma_H}{\sigma_v}$ and $k_h = \frac{\sigma_h}{\sigma_v}$, where σ_H and σ_h are the maximum and minimum principal horizontal stresses respectively. Depending on the sign and relative magnitudes of k_H and k_h, a normal, strike-slip or reverse stress regime is modelled. Angle θ is defined as the orientation of σ_H measured clockwise from north. In our simulations, k_H, k_h and θ are also unknowns of the multiparametric inversion process. In addition, an elastic half-space is used to take into account the traction-free effect of the Earth surface.

The inversion process is constrained by the mapped eruptive fissures from Chadwick & Howard (1991) and updated by the authors with the interpretation of more recent satellite images available on Google Earth in the southern area of Isabella Island (see Fig. 7). As we assumed that the eruptive fissures represent the strikes of the underlying dykes and that no information is available regarding the dip of the dykes, only the strike of the fissures is used to constrain the inversion. Because the topography has not been included in our simulations, the eruptive fissures, measured on the volcano flanks, are projected onto a horizontal surface at −600 m elevation where a horizontal observation grid covering the two islands is placed.

The modelled dyke orientations on the observation grid are derived from the computed stress field, and are used to compare

Table 1. Ellipsoid parameters of the seven magma chambers with a ratio of the longest axis over the vertical axis equal to 3.9 for all magma chambers

Magma chamber	Short axis (m)	Long axis (m)	Long axis orientation
Ecuador	3450	3450	/
Wolf	5680	6830	N162°
Darwin	5220	5220	/
Fernandina	5600	6760	N113°
Alcedo	4960	6150	N112°
Sierra Negra	6920	9250	N80°
Cerro Azul	4340	5350	N120°

Table 2. Inverted excess magma pressure p_e on the seven Galapagos volcanoes

Magma chamber	Pressure p_e (MPa)
Ecuador	8.69
Wolf	9.30
Darwin	8.55
Fernandina	9.60
Alcedo	5.25
Sierra Negra	9.15
Cerro Azul	6.60

with the observed pattern of eruptive fissures. The objective function used for the simulation is that described earlier for opening-mode fractures.

In the following mechanical simulations, we use a homogeneous linear elastic and isotropic behaviour characterized by two constants, Poisson's ratio and Young's Modulus. We use a value of 0.25 for Poisson's ratio (ν) and 30 GPa for Young's Modulus (E), which are the mean values representative for the surrounding rock.

3.b.2. Galapagos inversion results

The multiparametric inversion, which consists of 12 pre-computed simulations and 30 000 random geomechanical simulations (see Supplementary Material 4, available online at https://doi.org/10.1017/S001675682200067X), gives the optimum solution with a mean misfit angle $\bar{\delta} = 13.6°$, between the orientation of the observed and the modelled dykes, which varies from 0° (best fit) to 90° (worst fit). The optimum solution also gives a far field maximum horizontal stress (σ_H) oriented N89°E and a normal stress regime where $k_H = 0.381$ and $k_h = 0.378$. This is very close to a uniaxial normal stress regime where $\sigma_H = \sigma_h$. It is difficult to relate these inverted regional stress parameters to the actual stress field as very little is known about present-day stresses in the Galapagos.

The inverted magma excess pressures (p_e) for each volcano are shown in Table 2. The excess pressure at the time of dyke propagation is normally equal to the tensile strength of the host rock and is generally in the range of 0.5–6 MPa, up to about 9 MPa (Gudmundsson, 2012). This pressure can be negative when there is a deflation of the magma chamber or collapse of the caldera. The inverted p_e for all volcanoes are all positive (i.e. excess pressure) and fall within the range of tensile strength of the host rock with the smallest $p_e = 5.25$ MPa for Alcedo volcano (one of the least active) and the highest $p_e = 9.6$ MPa for Fernandina volcano (one of the most active).

The optimum solution found from the multiparametric inversion is illustrated by the histogram of the misfit angles (δ), computed at each dyke segment (Fig. 9a). The histogram shows a rapid decay with increasing δ. Of the observed eruptive fissures, 69.4% have a δ that is less than 15° with the modelled dykes.

Figure 9b shows a qualitative comparison between the observed pattern and the modelled dyke trajectories derived from the perturbed stress field. The modelled dyke trajectories show a good correspondence with the observed pattern of eruptive fissures. On the volcano flanks, the modelled and observed dyke trajectories converge toward the summit calderas, forming a well-defined radial pattern. On Fernandina Island the radial dykes tend to deviate

from a purely radial trend at some distance from the caldera (i.e. 15 km). Their orientation may be affected by the regional stress field to the west and may be more affected by the nearby Darwin and Alcedo volcanoes to the east. The latter effect is even more pronounced between the Alcedo, Darwin, Wolf and Ecuador volcanoes where modelled and observed radial dykes show a continuous curving trend illustrating the clear mechanical interaction between contemporaneous volcanoes. The modelled dyke trajectories show several unique points where the orientation is not defined (orange dots in Fig. 9). These points, called isotropic stress points where local $\sigma_h = \sigma_H$, are typical of perturbed stress field from several sources (i.e. magma chambers). Overall, there is not a very discernible effect of the regional stress on the modelled dyke trajectories as we are very close to a uniaxial normal stress regime where far field horizontal stress $\sigma_h \approx \sigma_H$.

The modelled dyke trajectories display a systematic circumferential dyke pattern above all the modelled magma chambers as observed in the field (Chadwick & Howard, 1991). The presence of both radial and circumferential dykes in the geomechanical model illustrates that the development of both types of dykes can be contemporaneous as suggested by Chadwick and Howard (1991) and Chadwick and Dieterich (1995) from field observation and modelling respectively. Figure 10 illustrates the 3D nature of the modelled dyke trajectories over the Fernandina magma chamber. Since dykes (i.e. opening-mode fractures) propagate in a plane normal to the local direction of the least compressive stress (i.e. σ_3), we represent the modelled dyke orientation as yellow discs (Fig. 10) whose normal is aligned with the local least compressive stress direction. The radial dykes are mostly but not exclusively sub-vertical in this case. However, the modelled circumferential dykes just above the magma chamber are dipping inward toward the caldera as observed in the field (Chadwick & Howard, 1991).

4. Discussion and conclusion

We use the boundary element method (BEM) to numerically invert for key magmatic and tectonic model parameters, based on the observed pattern of dyke intrusions surrounding magma chambers. Inverting for both the far field stress and the pressure in magma chambers implies that we must account for the volumetric change. Therefore, we extended the standard formulation of stress inversion by introducing a normalized volumetric stress ratio (R_v) in addition to the classical stress ratio, renamed as shear stress ratio (R_s) for clarity. In addition to R_v, magma pressure is also introduced into the stress inversion formulation. The magma pressure can be decomposed into an isotropic pressure gradient (Yun *et al.* 2006; Gudmundsson, 2012) and an excess pressure,
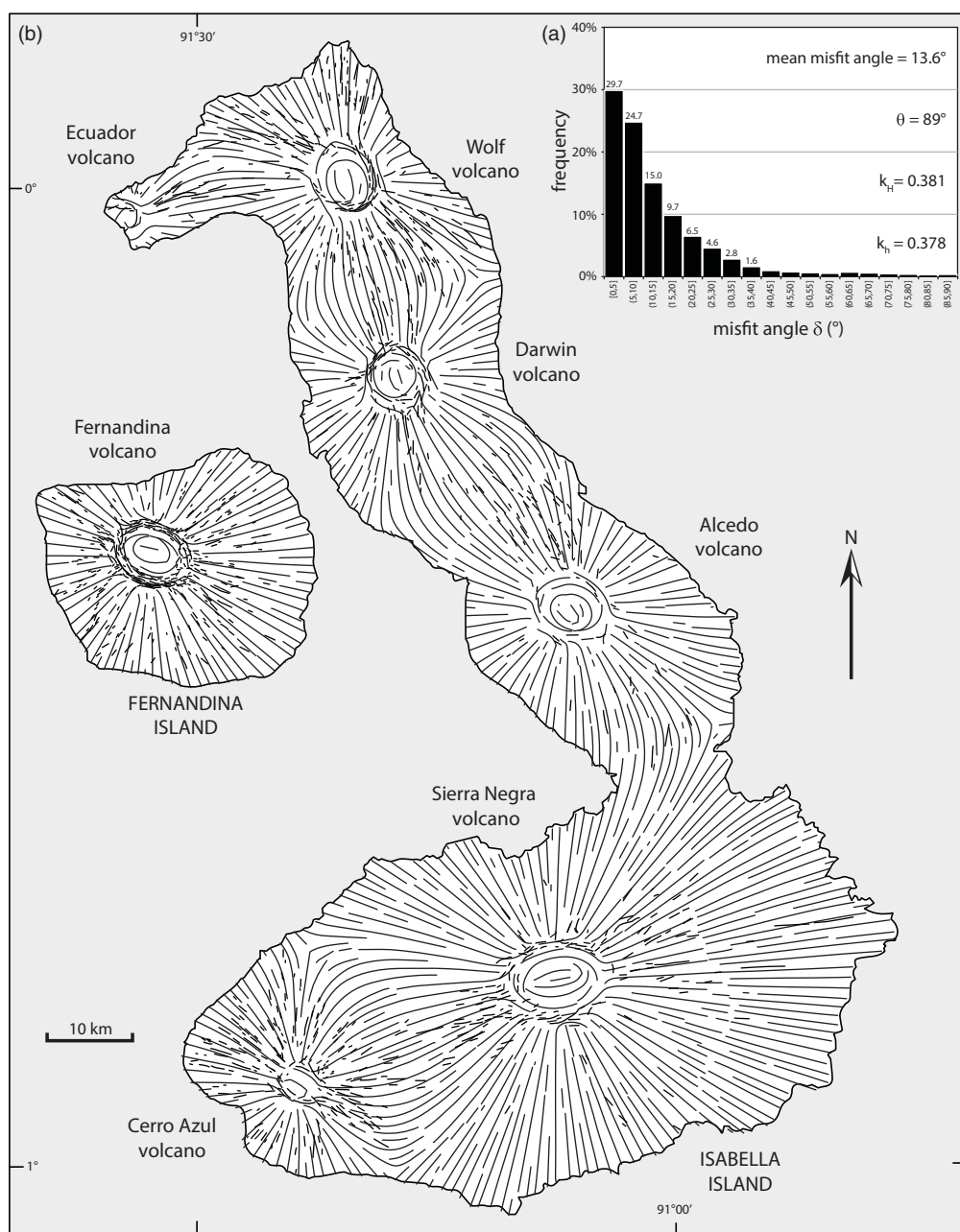
Fig. 9. (a) Histograms of the misfit angles (δ) for the optimum model parameters. (b) Map of observed eruptive fissures (thick black lines) and modelled dyke trajectories (thin black lines) for the optimum Galapagos model parameters. Circles highlight the location of computed isotropic stresses where dyke trajectories cannot be defined.

that is, a pressure in excess of isotropic stress at the depth of the magma chamber (Pollard, 1987; Lister, 1990; Rubin, 1995; Rubin & Gillard, 1998; Segall, 2010; Gudmundsson, 2011, 2020). Magma pressure is a critical parameter to be inverted that is locally competing with the far field tectonic stress. The magma pressure is thus added to the initial normal traction on the inner surface of the pressurized discontinuities. Using the superposition principle (Maerten, 2010a; F Maerten *et al.* 2016; L Maerten *et al.* 2016) and a Monte Carlo inversion minimizing some objective functions, this technique can explore the entire solution space. In addition, this technique could potentially use combined different datasets to constrain the inversion, such as focal mechanisms, InSAR, GPS, fracture type and orientation, fault-slip and tiltmeter data.

The linear elastic assumption necessary to use the principle of superposition in the proposed method might appear too restrictive. Indeed, non-linear behaviour such as plasticity is not considered here. However, although it is known that local plastic deformation occurs when stresses reach the elastic limit near a source of deformation, this should not affect our modelling approach. Indeed, most observations of dyke orientations found in the literature are far away (i.e. hundreds of metres or kilometres) from magma chambers, thus, far from any plastic deformations that would occur adjacent to these chambers.

It is important to note that viscous magma behaviour is not modelled explicitly, only the boundary conditions at the surface of the magma chambers account for its static behaviour. Therefore, the proposed inversion technique, like most of the other

Fig. 10. 3D perspective view of observed eruptive fissures at the surface (thick black lines), used to constrain the inversion, and modelled dyke orientations (yellow discs) above the Fernandina magma chamber (red ellipsoid). The modelled radial dykes are sub-vertical while the modelled circumferential dykes dip toward the magma chamber.
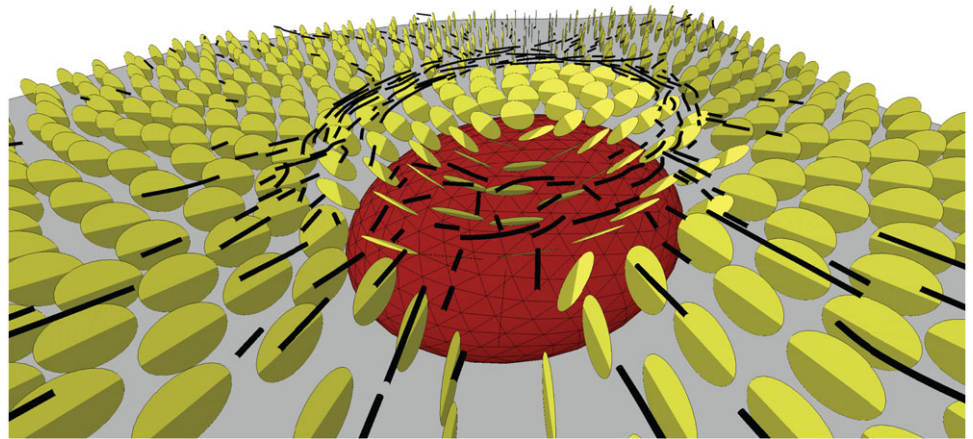
stress inversion techniques, assumes that the observed dykes or eruptive fissures represent a snapshot in time that can be statically modelled.

As stated earlier, this method is based on the postulate that dyke trajectories must have followed the past ambient stresses that are a combination of local stresses near pressurized magma chamber and far field tectonic stresses. It is therefore assumed that no other important mechanisms must have constrained the observed dyke propagation paths. For instance, anisotropic materials (e.g. layering) could also contribute to the heterogeneous ambient stress. It is also argued that pre-existing natural fractures could deviate dyke paths from the ambient stresses. However, while some dykes use fractures (e.g. faults) as parts of their paths, the conditions when this happens are well understood and rarely met (Gudmundsson, 2020). Field observations show that the great majority of dykes and inclined sheets are pure opening-mode fractures (Bistacchi *et al.* 2012).

Although, several 3D numerical methods can be used with this inversion methodology, such as the finite element method (FEM) or the finite difference method (FDM), we have decided to use the boundary element method (BEM) because it presents some technical advantages. For instance, BEM does not suffer from model edge effects as in FEM or FDM, for which model boundaries must be extended far from the zone of interest. BEM can optionally be used assuming a half-space or non-flat surface topography (Martel, 2000; Griffith *et al.* 2014) to model traction-free surface of the Earth. Another particular benefit of BEM is that overlapping, opening and shearing displacements along discontinuity walls can be explicitly modelled (Maerten *et al.* 2014) and the associated displacement, strain and stress fields can be computed everywhere in the 3D space without any topological support. Finally, with BEM only the 3D surfaces representing displacement discontinuities such as fractures, cavities, intrusions, bedding interfaces and magma chambers have to be defined as triangulated surfaces. This also allows for faster and easier building and editing of complex 3D models. This feature will also be very useful for easily and automatically editing magma chamber shapes and locations in non-linear geometry inversion processes.

Nevertheless, BEM has two main limitations regarding its use for the proposed multiparametric inversion method. First, anisotropic materials are hard to implement and would be very time- and memory-intensive. Yet, heterogeneous materials and/or layer boundary discontinuities can be used to model anisotropy caused by layering (Maerten & Maerten, 2008) while the volume of the model does not have to be built and meshed explicitly. The second main limitation is that the system matrix to solve is dense compared to other methods. Consequently, the memory needed and the time to numerically solve a problem are at least quadratic. Optimization techniques exist to optimize the matrix construction and the resolution time (Maerten, 2010*b*), but generally BEM can be more demanding than other methods, even for linear elastic behaviour.

We applied the inversion to two natural examples of volcanoes with well-developed dyke swarms. For the Spanish Peaks model, the method was used to invert for three parameters: the ratio of the two horizontal principal stresses, the orientation of the maximum horizontal principal stress and the excess pressure in the magma chamber. Weighted data were used to better constrain the inversion, and the results clearly show the interaction between the far field stress and local magmatic pressure to explain the observed dyke trajectories. In this modelling, the strike and dip of the observed dykes were used to constrain the inversion.

The Galapagos model, which is more complex compared to the Spanish Peaks case, shows that it is possible to invert for seven different excess pressures in addition to the far field stresses. The inversion was able to estimate 12 unknown physical parameters. In this modelling, only traces of the dykes (i.e. eruptive fissures) were used to constrain the inversion and no assumption was made about the dip angle of the underlying dykes. The simulation confirms that circumferential and radial dykes form within the perturbed stress field due to the interaction of far field stress and pressure in local magma chambers (Chadwick & Dieterich, 1995). It also provides a possible geometry for the underlying dykes which tend to be sub-vertical for the radial dykes and dipping towards the magma chamber for the circumferential dykes.

We propose that this method opens new opportunities to perform non-linear inversions for the shape and position of magma chambers in addition to the far field stress, excess pressures and magma densities. This non-linear inversion could also take advantage of using multiple types of both past data (dyke trajectories, fracture orientations, fault slip) and contemporary data (GPS, InSAR, tiltmeters) and could open new ways to investigate past and future eruptions.

References

Anderson EM (1905) The dynamics of faulting. *Transactions of the Edinburgh Geological Society* **8**, 387–402.

Anderson EM (1951) *The Dynamics of Faulting and Dyke Formation with Applications to Britain*, 2nd edition. Edinburgh: Oliver and Boyd, 206 pp.

Angelier J (1979) Néotectonique de l'arc Égéen. PhD thesis, Université Pierre et Marie Curie, Paris. Published thesis

Angelier J (1994) Fault slip analysis and palaeostress reconstruction. In *Continental Deformation* (eds WM Dunne and PL Hancock), pp. 53–100. Oxford: Pergamon Press.

Angelier J (2002) Inversion of earthquake focal mechanisms to obtain the seismotectonic stress-IV: a new method free of choice among nodal planes. *Geophysical Journal International* **150**, 588–609.

Armstrong RL (1969) K-Ar dating of Laccolithic centers of the Colorado Plateau and vicinity. *Geological Society of America Bulletin* **80**, 2081–6.

Baer G and Reches Z (1991) Mechanics of emplacement and tectonics implications of the Ramon dike system, Israel. *Journal of Geophysical Research* **96**, 11895–910.

Bauve V, Plateaux R, Rolland Y, Sanchez G, Bethoux N, Delouis B and Darnault R (2014) Long-lasting transcurrent tectonics in SW Alps evidenced by Neogene to present-day stress fields. *Tectonophysics* **621**, 85–100.

Bazargan M and Gudmundsson A (2019) Dike-induced stresses and displacements in layered volcanic zones. *Journal of Volcanology and Geothermal Research* **384**, 189–205.

Bazargan M and Gudmundsson A (2020) Stresses and displacements in layered rocks induced by inclined (cone) sheets. *Journal of Volcanology and Geothermal Research* **401**, 106965.

Bergerat F (1987) Stress fields in the European platform at the time of Africa-Eurasia collision. *Tectonics* **6**, 99–132.

Bistacchi A, Tibaldi A, Pasquar FA and Rust D (2012) The association of cone-sheets and radial dykes: data from the Isle of Skye (UK), numerical modelling, and implications for shallow magma chambers. *Earth and Planetary Science Letters* **339–340**, 46–56.

Bourne SJ and Willemse EJM (2001) Elastic stress control on the pattern of tensile fracturing around a small fault network at Nash Point, UK. *Journal of Structural Geology* **23**, 1753–70.

Brillouin L (1946) *Wave Propagation in Periodic Structures: Electric Filters and Crystal Lattices*. New York: McGraw-Hill.

Browning J and Gudmundsson A (2015) Caldera faults capture and deflect inclined sheets: an alternative mechanism of ring dyke formation. *Bulletin of Volcanology* **77**, 1–13.

Célérier B, Etchecopar A, Bergerat F, Vergely P, Arthaud F and Laurent P (2012) Inferring stress from faulting: from early concepts to inverse methods. *Tectonophysics* **581**, 206–19.

Chadwick WW and Dieterich JH (1995) Mechanical modeling of circumferential and radial dyke intrusion on Galapagos volcanoes. *Journal of Volcanology and Geothermal Research* **66**, 37–52.

Chadwick WW and Howard KA (1991) The pattern of circumferential and radial eruptive fissures on the volcanoes of Fernandina and Isabela islands, Galapagos. *Bulletin of Volcanology* **53**, 259–75.

Chestler SR and Grosfils EB (2013) Using numerical modeling to explore the origin of intrusion patterns on Fernandina volcano, Galapagos Islands, Ecuador. *Geophysical Research Letters* **40**, 4565–9.

Corbi F, Rivalta E, Pinel V, Maccaferri F, Bagnardi M and Acocella V (2015) How caldera collapse shapes the shallow emplacement and transfer of magma in active volcanoes. *Earth and Planetary Science Letters* **431**, 287–93.

De Joussineau G, Petit J-P and Gauthier BD (2003) Photoelastic and numerical investigation of stress distributions around fault models under biaxial compressive loading conditions. *Tectonophysics* **363**, 19–43.

Dorigo M (1992) *Optimization, Learning and Natural Algorithms*. PhD thesis, Politecnico di Milano, Milan. Published thesis.

Etchecopar A, Vasseur G and Daignieres M (1981) An inverse problem in microtectonics for the determination of stress tensors from fault striation analysis. *Journal of Structural Geology* **3**, 51–65.

Fjaer E, Holt RM, Horsrud P and Raaen AM (2008) *Petroleum Related Rock Mechanics*. Amsterdam: Elsevier.

Geist DJ, McBirney AR and Duncan RA (1986) Geology and petrogenesis of lavas from San Cristobal Island, Galapagos Archipelago. *Geological Society of America Bulletin* **97**, 555–66.

Griffith WA, Becker J, Cione K, Miller T and Pan E (2014) 3D topographic stress perturbations and implications for ground control in underground coal mines. *International Journal of Rock Mechanics and Mining Sciences* **70**, 59–68.

Gudmundsson A (2011) Deflection of dykes into sills at discontinuities and magma-chamber formation. *Tectonophysics* **500**, 50–64.

Gudmundsson A (2012) Magma chambers: formation, local stresses, excess pressures, and compartments. *Journal of Volcanology and Geothermal Research* **237–238**, 19–41.

Gudmundsson A (2020) *Volcanotectonics*. Cambridge: Cambridge University Press.

Gudmundsson A and Andrew REB (2007) Mechanical interaction between active volcanoes in Iceland. *Geophysical Research Letters* **34**, 1–5.

Hills RC (1901) *Description of the Spanish Peaks quadrangle, Colorado. US Geological Survey Geologic Atlas of the United States*, Folio 71, 7 pp. Denver, CO: US Geological Survey.

Jaeger JC, Cook NG and Zimmerman R (2009) *Fundamentals of Rock Mechanics*. Chichester: John Wiley & Sons.

Johnson RB (1961) Patterns and origin of radial dyke swarms associated with West Spanish Peak and Dyke Mountain, south-central Colorado. *Geological Society of America Bulletin* **72**, 579–90.

Johnson RB (1968) *Geology of the igneous rocks of the Spanish Peaks region, Colorado. US Geological Survey Professional Paper* 594-G, 47 pp.

Jolly RJH and Sanderson DJ (1995) Variation in the form and distribution of dykes in the Mull swarm, Scotland. *Journal of Structural Geology* **17**, 1543–57.

Kattenhorn SA, Aydin A and Pollard DD (2000) Joints at high angles to normal fault strike: an explanation using 3D numerical models of perturbed stress fields. *Journal of Structural Geology* **22**, 1–23.

Kaven J, Maerten F and Pollard DD (2011) Mechanical analysis of fault slip data: implications for paleostress analysis. *Journal of Structural Geology* **33**, 78–91.

Knopf A (1936) Igneous geology of the Spanish Peaks region, Colorado. *Bulletin of the Geological Society of America* **47**, 1727–84.

Lisle RJ, Orife TO, Arlegui L, Liesa C and Srivastava DC (2006) Favoured states of paleostress in the earth's crust: evidence from fault-slip data. *Journal of Structural Geology* **28**, 1051–66.

Lister JR (1990) Buoyancy-driven fluid fracture: similarity solutions for the horizontal and vertical propagation of fluid-filled cracks. *Journal of Fluid Mechanics* **217**, 213–39.

Luo G, Nikolinakou MA, Flemings PB and Hudec MR (2012) Geomechanical modeling of stresses adjacent to salt bodies. Part 1 – Uncoupled models. *AAPG Bulletin* **96**, 43–64.

Maccaferri F, Bonafede M and Rivalta E (2011) A quantitative study of the mechanisms governing dyke propagation, dyke arrest and sill formation. *Journal of Volcanology and Geothermal Research* **208**, 39–50.

Maerten F (2010a) *Geomechanics to solve geological structure issues: forward, inverse and restoration modeling*. Université Montpellier II, Sciences et techniques du Languedoc, Montpellier. Published thesis.

Maerten F (2010b) Adaptive cross-approximation applied to the solution of system of equations and post-processing for 3D elastostatic problems using the boundary element method. *Engineering Analysis with Boundary Elements* **34**, 483–91.

F Maerten *et al.*

Maerten F, Madden EH, Pollard DD and Maerten L (2016) Incorporating fault mechanics into inversions of aftershock data for the regional remote stress, with application to the 1992 Landers, California earthquake. *Tectonophysics* **674**, 52–64.

Maerten F and Maerten L (2008) Iterative 3D BEM solver on complex faults geometry using angular dislocation approach in heterogeneous, isotropic elastic whole or half-space. *Skerget and Brebbia Editors, Boundary Elements and other Mesh Reduction Methods* **30**, 201–208.

Maerten F, Maerten L and Pollard DD (2014) iBem3D, a three-dimensional iterative boundary element method using angular dislocations for modeling geologic structures. *Computers & Geosciences* **72**, 1–17.

Maerten F, Resor P, Pollard DD and Maerten L (2005) Inverting for slip on three-dimensional fault surfaces using angular dislocations. *Bulletin of the Seismological Society of America* **95**, 1654–65.

Maerten L (2000) Variation in slip on intersecting normal faults: implications for paleostress inversion. *Journal of Geophysical Research: Solid Earth* **105**, 25553–65.

Maerten L, Maerten F and Lejri M (2018) Along fault friction and fluid pressure effects on the spatial distribution of fault-related fractures. *Journal of Structural Geology* **108**, 198–212.

Maerten L, Maerten F, Lejri M and Gillespie P (2016) Geomechanical paleostress inversion using fracture data. *Journal of Structural Geology* **89**, 197–213.

Maerten L, Pollard DD and Karpuz R (2000) How to constrain 3-D fault continuity and linkage using reflection seismic data: a geomechanical approach. *AAPG Bulletin* **84**, 1311–24.

Martel SJ (2000) Modeling elastic stresses in long ridges with the displacement discontinuity method. *Pure and Applied Geophysics* **157**, 1039–57.

McBirney AR and Williams H (1969) Geology and petrology of the Galapagos Islands. *Geological Society of America, Memoir* **118**, 197 pp.

Michael AJY (1984) Determination of stress from slip data: faults and folds. *Journal of Geophysical Research* **89**, 11517–26.

Michael JAY (1987) Use of focal mechanisms to determine stress: a control study. *Journal of Geophysical Research* **92**, 357–68.

Mogi K (1959) Relations between the eruptions of various volcanoes and the deformations of the ground surfaces around them. *Bulletin of Earthquakes Research Institute, University of Tokyo* **36**, 99–134.

Muller OH (1986) Changing stresses during emplacement of the radial dyke swarm at Spanish Peaks, Colorado. *Geology* **14**, 157–9.

Muller OH and Pollard DD (1977) The stress state near Spanish Peaks, Colorado, determined from a dyke pattern. *Pure and Applied Geophysics* **115**, 69–86.

Munro AC and Rowland SK (1996) Caldera morphology in the western Galapagos and implications for volcano eruptive behavior and mechanisms of caldera formation. *Journal of Volcanology and Geothermal Research* **72**, 85–100.

Nakamura K, Jacob KH and Davies JN (1977) Volcanoes as possible indicators of tectonic stress orientation – Aleutians and Alaska. *Pure and Applied Geophysics* **115**, 87–112.

Nikkhoo M and Walter TR (2015) Triangular dislocation: an analytical, artefact-free solution. *Geophysical Journal International* **201**, 1119–41.

Nordlie E (1973) Morphology and structure of the Western Galapagos volcanoes and a model for their origin. *Geological Society of America Bulletin* **84**, 2931–56.

Odé H (1957) Mechanical analysis of the dyke pattern of the Spanish Peaks area, Colorado. *Geological Society of America Bulletin* **68**, 567–76.

Okada Y (1992) Internal deformation due to shear and tensile faults in a half-space. *Bulletin of the Seismological Society of America* **82**, 1018–40.

Pham DT, Ghanbarzadeh A, Koc E, Otri S, Rahim S and Zaidi M (2005) *The Bees Algorithm*. Technical Note. Cardiff: Manufacturing Engineering Centre, Cardiff University.

Pinel V and Jaupart C (2004) Magma storage and horizontal dyke injection beneath a volcanic edifice. *Earth and Planetary Science Letters* **221**, 245–62.

Plateaux R, Béthoux N, Bergerat F and de Lépinay BM (2014) Volcano-tectonic interactions revealed by inversion of focal mechanisms: stress field insight around and beneath the Vatnajökull ice cap in Iceland. *Frontiers in Earth Science* **2**, 9 pp.

Pollard DD (1987) Elementary fracture mechanics applied to the structural interpretation of dykes. In *Mafic Dyke Swarms* (eds HC Halls and WF Fahrig), pp. 5–24. Toronto: Geological Association of Canada, Special Paper no. 34.

Pollard DD and Muller OH (1976) The effect of gradients in regional stress and magma pressure on the form of sheet intrusions in cross section. *Journal of Geophysical Research* **81**, 975–84.

Rivalta E, Taisne B, Bunger AP and Katz RF (2015) A review of mechanical models of dyke propagation: schools of thought, results and future directions. *Tectonophysics* **638**, 1–42.

Rubin AM (1995) Propagation of magma-filled cracks. *Annual Review of Earth and Planetary Sciences* **23**, 287–336.

Rubin AM and Gillard D (1998) Dyke-induced earthquakes: theoretical considerations. *Journal of Geophysical Research: Solid Earth* **103**, 10017–30.

Segall P (2010) *Earthquake and Volcano Deformation*. Princeton, New Jersey: Princeton University Press.

Sigmundsson F, Hooper A, Hreinsdóttir S, Vogfjörd KS, Ófeigsson BG, Heimisson ER, Dumont S, Parks M, Spaans K, Gudmundsson GB, Drouin V, Árnadóttir T, Jónsdóttir K, Gudmundsson MT, Högnadóttir T, Fridriksdóttir HM, Hensch M, Einarsson P, Magnússon E and Eibl EPS (2014) Segmented lateral dyke growth in a rifting event at Bárðarbunga volcanic system, Iceland. *Nature* **517**, 191–5.

Smith RP (1975) *Structure and Petrology of Spanish Peaks Dykes, South-Central Colorado*. Boulder: University of Colorado, Boulder. Published thesis.

Smith RP (1978) *Geologic maps of part of the Spanish Peaks dyke system, south-central Colorado*. Denver, CO: Geological Survey of America Map and Chart Series MC-22, scale 1:36000, 1 sheet, 2 pp. text.

Soliva R, Maerten F, Petit J-P and Auzias V (2010) Field evidences for the role of static friction on fracture orientation in extensional relays along strike slip faults: comparison with photoelasticity and 3-D numerical modelling. *Journal of Structural Geology* **32**, 1721e1731.

Stormer JC (1972) Ages and nature of volcanic activity on the southern high plains, New Mexico and Colorado. *Geological Society of America Bulletin* **83**, 2443–8.

Thomas AL (1993) *Poly3D, a three-dimensional, polygonal-element, displacement discontinuity boundary element computer program with applications to fractures, faults, and cavities in the earth's crust*. Master Thesis at Stanford University.

Yamakawa N (1955) On the strain produced in a semi-infinite elastic solid by an interior source of stress. *Journal of the Seismological Society Japan* **8**, 84–98.

Yun S, Segall P and Zebker H (2006) Constraints on magma chamber geometry at Sierra Negra Volcano, Galapagos Islands, based on InSAR observations. *Journal of Volcanology and Geothermal Research* **150**, 232–43.